In Situ Analysis of NMC|graphite Li-Ion Batteries by Means of Complementary Electrochemical Methods

Journal of The Electrochemical Society, 2020 **167** 090528

In Situ Analysis of NMC|graphite Li-Ion Batteries by Means of Complementary Electrochemical Methods

Imanol Landa-Medrano,[1] Aitor Eguia-Barrio,[1] Susan Sananes-Israel,[1] Silvia Lijó-Pando,[1] Iker Boyano,[1] Francisco Alcaide,[1] Idoia Urdampilleta,[1] and Iratxe de Meatza[1,2,z]

[1]*CIDETEC, Basque Research and Technology Alliance (BRTA), 20014 Donostia-San Sebastián, Spain*
[2]*Inorganic Chemistry Department, Faculty of Science and Technology, University of the Basque Country, UPV/EHU, 48080 Bilbao, Spain*

Lithium-ion technology is considered as outstanding candidate for implementation in high energy density applications. Adjusting the cycling conditions of electrodes and monitoring the undergoing reactions are necessary to maximize their potentiality and ensure high performance and safe operation for end-users. Herein, in situ electrochemical impedance spectroscopy (EIS), direct current (DC) resistance and differential voltage analysis (DVA) are complementarily used to understand and predict the lifetime of $LiNi_{0.6}Mn_{0.2}Co_{0.2}O_2$ (NMC622) vs graphite coin cells cycled at different upper cut-off voltage (UCV). Lithium de/intercalation reactions in graphite, phase transitions in NMC and the formation of electrode-electrolyte interphases have been identified by DVA. Combined with EIS and DC resistance, the occurrence of these reactions has been monitored upon cycling. The main findings indicate that despite observing other detrimental phenomena (charge transfer resistance increase or irreversibility of NMC622 phase transitions), the different solid electrolyte interphase (SEI) formation and resistance with UCV are most relevant factors affecting cycle life. The loss of lithium inventory is the main cause of the capacity fade. The need of a stable SEI to delay the continuous electrolyte consumption is highlighted. The combined information provided by these techniques can be leveraged by battery management systems to optimize cell performance while cycling.
 [DOI: 10.1149/1945-7111/ab8b99]

Manuscript submitted February 11, 2020; revised manuscript received April 17, 2020. Published April 29, 2020. *This paper is part of the JES Focus Issue on Battery Safety, Reliability and Mitigation.*

Supplementary material for this article is available online

The objective of minimizing the carbon emissions from the combustion of fossil fuels, as close as possible from a zero-carbon emission world, is unachievable without being able to store the energy generated from renewable sources. Since their conception, Li-ion batteries (LIBs) have been identified as one of the principal energy storage solutions.[1] Nowadays, LIBs are found everywhere in developed countries (mobile phones, laptops) and because of their high specific energy density (both gravimetric and volumetric) this technology is considered as one of the most promising solutions to replace fossil fuels in the automotive field.[2] Before achieving this ambitious goal, however, LIBs still require an optimization of the energy density and an increase of the cycle life.[1,3,4]

In order to improve the energy and stability performance of this technology, many strategies have been discussed and experimented, such as the investigation of new active materials,[5–7] the electrolyte formulation[8,9] or the optimum working conditions.[10,11] However, the cell degradation with the cycle life is inherent to the material and it should be easily monitored in order to minimize it.[12] Degradation of the cells has also been investigated previously.[13–15] Regarding the developed positive electrode materials, layered oxides combining different transition metals have been significantly impactful.[16,17] In particular, those based on Ni, Mn and Co with the formula $LiNi_xMn_yCo_zO_2$ ($x + y + z = 1$) (NMC) show a reasonable compromise between energy density, cycling performance and safety.[1,16] Among the transition metals in this structure, Mn is responsible for the structural integrity of the compound, Ni for the charge compensation and Co for the stabilization of the layered structure.[18] The need for higher energy densities for automotive applications, nevertheless, promoted the increase in Ni content, which compromises the thermal, structural and cycling stability of the NMC material.[18] Furthermore, it has been observed that the increase of Ni in this layered material gradually leads to a heightened instability at high potentials upon cycling.[19] Briefly, it has been demonstrated that the higher the Ni content, the easiest oxygen atoms are removed from the crystal structure of NMC, ultimately leading to a worse electrochemical performance.[9,20]

On the other hand, the negative electrode usually consisting of graphite as the active material,[21,22] also presents challenges, usually, and paradoxically, related to the layer allowing its safety, power capability and cycling life: the solid electrolyte interface (SEI), which is formed at the negative electrode surface due to the reaction of the electrolyte with this electrode.[23] The formation of this layer occurs principally in the first galvanostatic cycle(s) and determines the performance of the battery during its cycle life, being therefore a field of significant interest for battery researchers.[24–27] It is necessary to form an stable SEI, as one of the main degradation mechanisms in LIBs, the so-called loss of lithium inventory (LLI), occurs due to the continuous consumption of the electrolyte to further form this layer upon the galvanostatic cycling.[21,28–30] Thus, multiple groups have focused their research on the optimization of the formation protocol.[26,31–33]

In this context, it is necessary to develop experimental techniques that allow the monitoring of the state of the batteries while cycling, in order to identify the degradation mechanism without the need of a time-consuming and complex post-mortem characterization.

The aim of this work is to present a combination of in situ electrochemical techniques to analyze the evolution of $LiNi_{0.6}Mn_{0.2}Co_{0.2}O_2$ (NMC622)|graphite Li-ion cells cycled under different testing parameters. The combined techniques allow the identification of phenomena, such as SEI growth, resistance evolution and lithium ion availability, applicable to all Li-ion cell formats. Differential Voltage Analysis (DVA)[21,29,34] at different State of Health (SOH) has been carried out to point out the evolution of the lithium ion availability upon cycle life. This method allows following the electrochemical redox reactions during cycling. Additionally, the measurement of capacity and coulombic efficiency (CE) combined with a pulse test is used to monitor the evolution of direct current (DC) resistance upon cycling.[35,28] Furthermore, Electrochemical Impedance Spectroscopy (EIS) has been used to

[z]E-mail: imeatza@cidetec.es

monitor the SEI growth in the negative electrode and the evolution of the different resistances in order to set the degradation mechanisms.[36–39] As a case of study, Li-ion full coin cells (FCCs) based on NMC622 positive electrodes and graphite negative electrodes are used to showcase the applicability of these combined test techniques. Herein, the electrodes are cycled setting different upper cut-off voltages (UCV), i.e. 4.1 V, 4.2 V and 4.3 V, and the influence of this condition onto the parameters analyzed by the different electrochemical techniques proposed is discussed within the existing literature. Even though the cell format (coin cell) and the single-coated electrodes are not ideal for monitoring commercial-quality electrodes, the techniques presented herein can be scaled-up to other cell formats and implemented to analyze commercially-available batteries.

Experimental

Electrode preparation.—Positive electrodes consisted of 90% NMC622 (Umicore) as active material, 5% carbon black C65 (Imerys) as conductive additive, and 5% poly-vinylidene fluoride (PVdF, Solef® 5130, Solvay) as binder. N-methyl pyrrolidone (NMP, Synthesis grade, Scharlab) was the solvent of the cathodic slurry. A water-based formulation was selected to prepare the negative electrodes, which consisted of 94% graphite (Hitachi HE3) as active material, 2% C45 (Imerys) carbon black as conductive agent, and 2% carboxymethyl cellulose (CMC, Walocel CRT2000, DOW) and 2% Styrene-Butadiene Rubber (SBR, BM451B, ZEON) as binders. Cathodic and anodic slurries were deposited onto Al (Hydro) and Cu (Furukawa) foils, respectively, at CIDETEC's electrode manufacturing pilot plant facilities, being later calendered to 2.7 g cm^{-3} (positive electrode) and 1.45 g cm^{-3} (negative electrode). The loading of the positive and negative electrodes was 3.1 and 3.35 mAh cm^{-2}, respectively. Electrodes were punched with EL-cut devices from EL-Cell in disk formats of 16.6 mm diameter in the case of the positive electrodes and 17.7 mm diameter for the negative electrodes in order to ensure the good alignment of the electrodes inside the cells. The value of 1 C in these electrodes was 6.7 mA. Electrodes were dried at 120 °C under vacuum inside the dry room with a dew point below −40 °C.

Electrochemical cell.—Coin cells (CR2025, Hohsen) were assembled inside the dry room. Electrodes were balanced for a negative/positive ratio of 10% of excess of capacity in the negative electrode. The commercial electrolyte used in this study was 1 mol dm^{-3} lithium hexafluorophosphate ($LiPF_6$) in ethyl carbonate (EC) and dimethyl carbonate (DMC) 1:1 plus 2% (weight percentage) of vinylidene carbonate (VC): 1 M $LiPF_6$ in EC:DMC (1:1 vol %) with 2%wt. VC (99.9% battery grade from Solvionic, reference E003). 75 μl of electrolyte were added to full and NMC622 coin cells, while 100 μl were added to the graphite coin cells. Celgard 2015 separator was selected for full and half coin cells with an NMC electrode, while the graphite half-coin cells (HCCs) were assembled with microfiber separator (Whatman). The use of the microfiber as separator allows the addition of higher volume of electrolyte. Therefore, it was the separator selected for graphite HCCs due to the presence of two electrodes forming their corresponding SEI (graphite and lithium), which involves higher electrolyte consumption. Finally, 50 μm thick lithium foil (Albemarle) was used as the counter and the reference electrode in HCC configuration.

Electrochemical measurements.—The assembled cells were characterized in a Basytec Cell Test System potentiostat at 25 °C ± 1 °C controlled by air conditioning. In addition, electrochemical impedance spectroscopy measurements were performed in a Potentiostat/Galvanostat PGSTAT30 equipped with a Frequency Response Analyzer (FRA2, N4L). Impedance spectra were fitted using Zview software version 3.5f (Scribner).

More in detail, formation of the cells consisted of a single galvanostatic cycle between the initial voltage of the cells, the upper cut-off voltage selected for each cell (4.1, 4.2 or 4.3 V) and a discharge to 2.7 V at C/20 for FCCs. On the other hand, potential windows were 0.01–1 V and 2.8–4.3 V for graphite- and NMC-based HCCs, respectively. After the formation cycle (and after allowing the cells to rest at OCV for 1 h), an impedance scan was performed between 10^6 and 10^{-3} Hz with a perturbation amplitude of 5 mV at 25 °C ± 1 °C. Then, the cells were galvanostatically cycled at C/3 following the three potential windows already mentioned until 80% of their state-of-health (SOH). Every 25 galvanostatic cycles, however, an impedance scan and a "check-up" analysis were conducted. Again, the cells were allowed to rest for 1 h before carrying out the impedance scan. This check-up consisted of a galvanostatic cycle at C/20 (which was used to perform differential voltage analysis), two cycles at C/2 and after setting the state-of-charge to 50%, a 1 C discharge pulse was applied (later used to calculate the DC resistance of the cell). After this check-up procedure the cell continued cycling for 25 cycles, until the next EIS and check-up block.

Post-mortem analyses.—After reaching 80% of SOH, cells were introduced in an Ar-filled glove box (MBraun) and disassembled inside ($[O_2] < 0.1$ ppm, $[H_2O] < 0.5$ ppm). The salts deposited onto the electrode surface were cleaned after cell disassembly using dimethyl carbonate prior to their post-mortem characterization. The influence of the electrochemical experiments on the NMC crystal structure was analyzed by means of powder X-ray diffraction (XRD), using a Bruker D8 Discover diffractometer (Cu Kα radiation, $\lambda = 0.154$ nm) equipped with a LynxEye PSD detector. The diffractograms were recorded between $2\theta = 10°$ and 85° at 0.003° s^{-1}, while the obtained data were fitted using the FULLPROF program.[40] In addition, the morphological evolution of the NMC622 electrodes was analyzed by field emission scanning electron microscope (FE-SEM, ULTRA plus ZEISS). X-ray photoelectron spectroscopy (XPS) was conducted to characterize the solid electrolyte interface formed on the surface of the graphite electrodes. ESCALAB 250Xi (Thermo Fisher Scientific) instrument with hemispherical analyzer (energy resolution: 0.1 eV, analysis area 0,65 mm) was employed. The X-ray source of such system was monochromated Al Kα (hν = 1486.68 eV) radiation, operated at 225 W, 15 kV. The XPS spectra were collected at pass energies 200 eV and 20 eV for survey spectra and individual elements respectively. Charge neutralization was achieved with both low energy electron and argon ion flood guns (0.5 eV, 100 μA and 70 μA current respectively) during XPS measurements. The XPS spectra were peak-fitted using Avantage processing software (Thermo Fisher Scientific). The Lorentzian/Gaussian line shape and "Smart" background subtraction were used for peak fitting. Quantification was done using sensitivity factors provided by the Avantage's library.

Results and Discussion

Formation test to follow the reactions in the first cycle.—FCCs assembled were initially subjected to the as-known formation cycle, which consisted of a charge-discharge cycle at C/10 C-rate, being the lower cut-off limit 2.7 V for all the cells, while the upper cut-off limit was set at 4.1, 4.2 and 4.3 V for the different cells studied. The main target of this formation cycle is to form a stable SEI that will permit a successful cycling performance.[32,41] The formation cycle of the cells, as well as the corresponding DVA (dQ/dV vs voltage) curve of one cell per UCV, are shown in Fig. 1.

As expected, the charge capacity in the formation increased with increasing the UCV; the average charge capacities achieved at 4.1, 4.2 and 4.3 V were 161.0 ± 6.7, 179.7 ± 0.5, 189.8 ± 4.2 mAh g^{-1}, respectively. Figure 1a shows the typical representation of the charge-discharge cycle, in which the cell was initially charged to the UCV and later discharged to 2.7 V. In this figure it is difficult to distinguish between the different reactions occurring at each voltage. In fact, it looks like the voltage increases gradually with the specific

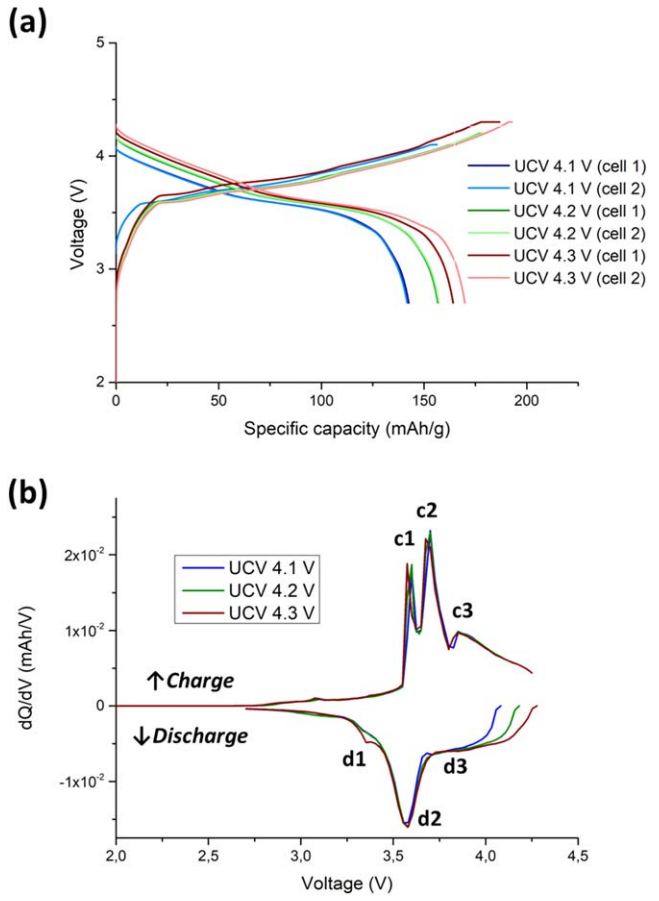

Figure 1. (a) Formation cycle of the cells with different upper cut-off potential: 4.1 (blue line), 4.2 (green line) and 4.3 V (red line). (b) dQ/dV vs voltage of the formation cycle of the LIBs.

capacity above 3.6 V. As mentioned, the charge of the cell was followed by the discharge, being possible to split the curve into three different regions: (i) below 3.4 V there was a marked capacity drop, (ii) between 3.4 and 3.6 V the slope of the curve was decreased and (iii) between the 3.6 V and UCV the voltage was linearly decreased with the capacity. The shape of these curves is similar to those that have been reported previously in the literature dealing with the use of Ni-rich NMC positive electrodes vs graphite negative electrodes.[17,19,21,29] Nevertheless, it is not that usual to further analyze the evolution of these reactions by deriving the capacity by the voltage, evidencing the potential at which more charge is passed though the cell. The first stages of the DVA of the charge reaction (Fig. 1b) reveal the first reactions starting at 2.8 V, before the redox reaction associated to the active materials in the electrode should take place. These reactions are ascribed in literature to the beginning of the SEI formation.[23,33] Afterwards, a first evident and sharp redox signal at 3.57 V (c1) followed by the main peak of the charge reaction at 3.70 V (c2) corresponding to the fraction of the charge plateau with the lowest slope in the galvanostatic curve. In addition, there is a third feature at 3.85 V (c3) after which the value of the rate of the reaction decreases progressively until the determined charge cut-off is reached. Even though no additional peaks were observed between 4.1 (lowest UCV) and 4.3 V (highest UCV), the dQ/dV value was higher than 0 and, therefore, electrochemical reactions occurred in this interval. As will be discussed later, these reactions will significantly condition the cell performance. In a recent work, Jung et al.[19] identified these processes in NMC|graphite cells. In their interpretation, c1 and c2 were ascribed to the lithiation of graphite ($C_6 \rightarrow LiC_x$) and the H1 → M (rhombohedral to monoclinic) transition of the NMC[42] (plus further lithiation of the graphite), respectively. On the other hand, in their work c3 peak was significantly less intense than observed here; it is worth mentioning that their scan corresponded to the third galvanostatic cycle, while in our case it is obtained from the first one. Furthermore, in the DVA of the subsequent cycles (as will be shown later) this contribution decreased and was shifted to higher potentials, taking a similar shape to that reported by Jung and coworkers,[19] which was associated with the M → H2 (monoclinic to rhombohedral) phase transition in the NMC.[42] Thus, it could be hypothesized that, apart from the later transition, additional reactions such as the formation of the SEI could be enhancing the c3 peak detected in the first scan as the formation of this protective layer is known to occur more significantly in the first charge of the LIBs. The absence of a marked peak at similar voltage in the subsequent discharge, and the appearance of a small feature (d3, maintained during the rest of the cycling life of the cell) support the hypothesis of the occurrence of irreversible reactions during the first charge. As these irreversible reactions are in good agreement with those responsible for the formation of the SEI and the cathode electrolyte interface (CEI), it could be concluded that more electrons were used for the formation of these layers as the selected UCV was higher.

Regarding the discharge reaction, two peaks were observed after the feature designed as d3 (corresponding to the reversible H2 → M phase transition of the NMC). On the one hand, a predominant signal, corresponding to the plateau in the galvanostatic discharge, was observed at 3.57 V (d2). This peak, appearing at the same voltage as c1, includes both the phase transition M → H1 and the delithiation of graphite, i.e. the inverse reactions to c1 and c2. Finally, it is also possible to distinguish a third signal at 3.35 V only for the cell previously charged to 4.3 V. Interestingly, this peak, also visible in Ref. 19 will be present for all the cells in the following cycles, regardless the charge cut-off. As the electrodes were balanced for a charge at 4.2 V, and for all the cases the negative electrode was in excess vs the positive one, it is likely that this feature could correspond to an additional delithiation of graphite. Its appearance in the discharge of the cell previously charged to 4.3 V and during the cycle life of all the cells could be ascribed to an offset of the practical potential windows of the NMC and the graphite.

To further prove the above assumptions, NMC622 vs Li and graphite vs Li HCCs were assembled. The formation cycles were performed in these two cells setting the potential window at 2.8–4.3 V and 0.01–1 V for the NMC622- and graphite-based HCCs, respectively. The aim was to calculate the resulting curve by combining the data of these two cells, leading to the chronopotentiogram and DVA representation of a FCC calculated by data subtraction (Fig. 2). In addition, the dQ/dV vs voltage representation of the half cells is displayed in Fig. S1 (available online at stacks.iop.org/JES/167/090528/mmedia). In good agreement with the former hypothesis, the peaks ascribed to the (de)intercalation of Li^+ from/into graphite (c1 and d1) are not observed. Furthermore, the open circuit voltage of the cell as-assembled was 3.45 V vs Li^+/Li (3.35 V vs graphite), corresponding to a fully lithiated NMC622 vs a lithium foil. Thus, the appearance of a feature at 3.35 V in the FCC must be ascribed to the negative electrode.

As can be observed in Fig. 2, the formation curves obtained by data manipulation from the graphite- and NMC-based HCCs have the same shape as those obtained in FCCs. This curve refers to the difference $E_{NMC}-E_{graphite}$. As a consequence, all the features present in the dQ/dV vs voltage curves of the real FCCs can be found in the calculated FCC curves. It is also worth commenting on the lithiation stages of graphite as it has been a research topic widely discussed in the battery community.[43–46] Starting from unlithiated graphite, lithium is initially introduced in its layered structure, leading to the LiC_{36} formation. This last phase is formed after a plateau at ~0.20 V, as determined by Levi and Aurbach[46] by means of cyclic voltammetry. In the next stage, lithiation of graphite continues until the formation of LiC_{27}. With further lithiation, LiC_{12} and LiC_6 are formed at 0.11 and 0.07 V, respectively. These stages are visible at extremely low current densities, but they are not easily discernible at

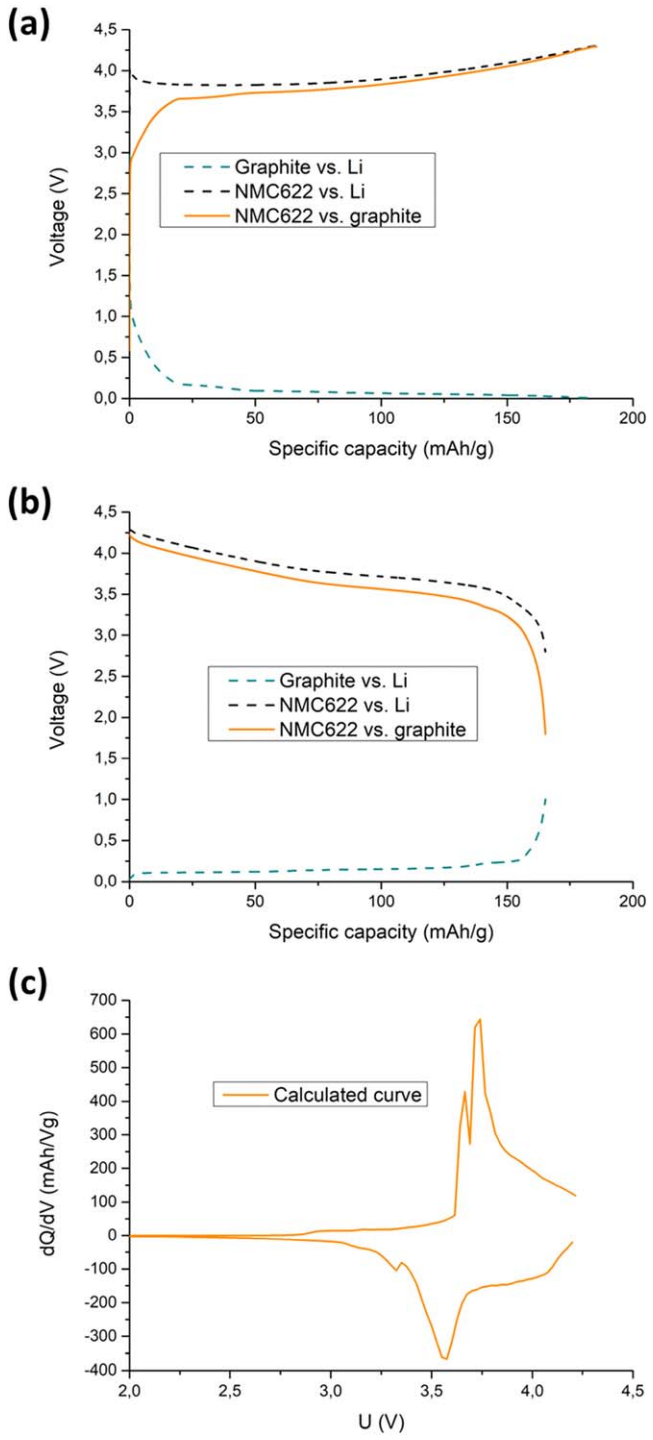

Figure 2. FCC formation curves obtained by the data manipulation of graphite and NMC622 HCCs ($E_{NMC}-E_{graphite}$). (a) Charge and (b) discharge profiles and (c) DVA curves.

usual operating currents.[45] The overpotential of the LiC_{36} formation reaction is observable at a potential slightly lower than 0.2 V (see DVA in Fig. S1a), while the two steps of the lithiation from LiC_{27} to LiC_6 cannot be appreciated separately. On the subsequent delithiation, however, these two processes are differenciated, confirming the formation of the three lithiation phases for the graphite electrode in HCC.

All in all, the information that was obtained from the formation protocol was that, on the one hand, the achieved discharge capacity is larger when the UCV is increased, as expected. On the other hand, more interestingly, the DVA of the different cells permit to precisely identify and locate the reaction plateaus of both charge and discharge, as well as ascribe them to different electrochemical processes. The analysis of these features upon cycling will be useful to get further detail on the evolution of the reactions occurring in the Li-ion battery.

Cycling performance to monitor the evolution of the capacity.—The cells previously discussed in the formation section were cycled at C/3 between 2.7 V and the corresponding UCV until the cells reached the 80% of the SOH. The capacity delivered by the cells with the number of cycles is displayed in Fig. 3.

The cells charged to 4.1, 4.2 and 4.3 V achieved an average of 191, 286 and 254 cycles before reaching the 80% of their SOH, respectively (Fig. 3a). As expected, the capacity of the cells cycled to 4.1 V was lower than the rest from the beginning to the end of their cycle life (Fig. 3c). On the other hand, the cells providing the longest cycle life were those with the charge cut-off established at 4.2 V (Fig. 3a). Interestingly, the cells cycled up to 4.2 and 4.3 V showed a higher Coulombic efficiency than those cycled at UCV 4.1 V (Fig. 3b). Finally, it is worth mentioning that even though the cells with the UCV 4.2 V run for a higher number of cycles, those charged to 4.3 V provided a higher Li^+ de/intercalation (i.e. a higher cumulative discharge capacity) during their cycle life (Fig. S2). This highlights not only the necessity of determining appropriate conditions to ensure suitable performance of the batteries (not achieved with UCV = 4.1 V), but also establishing priorities depending on the final application (energy density vs cycling stability when UCV 4.2 and 4.3 V are compared). The decision on the best charge cut-off, nevertheless, is beyond the scope of this work. The following sections will provide a showcase of methods to diagnose the state of the battery during its cycling evolution and provide tools to in situ identify and monitor key processes occurring in LIBs based on layered oxides as positive electrodes and graphite as negative electrodes.

Pulse test to monitor the evolution of DC resistance.—The DC resistance of the cells was analyzed every 25 cycles. An initial cycle at C/20 was performed to determine the remaining capacity. After that, the cells were driven to 50% of SOC. Finally, a 1 C discharge pulse was applied for 30 s, causing a voltage drop (ΔV). The resistance of the cell was calculated on the basis of Ohm's law:

$$\Delta V = I \cdot R \qquad [1]$$

Thus, the resistance was calculated by substituting the voltage drop registered and the current applied (I) in Eq. 1. The DC resistance evolution for each cell with the SOH is shown in Fig. 4. These values have been represented as the resistance increase in Fig. 4 in order to minimize the effects of the coin cell casing, which can lead to significant differences between the coin cells.[47] This allowed us representing all together the resistance values calculated for the different cells, showing a quasi-linear trend between the DC resistance vs SOH. For the sake of interpretation, straight lines corresponding to the different UCVs have been included in Fig. 4, and they allow seeing whereas the resistance variation is very similar for the cells with UCV 4.1 and 4.2 V, is higher for the cells with UCV 4.3 V. This means that charging the cells to 4.3 V favors the occurrence of reactions that result in an increased DC resistance of the cells, which can lead to an increased overpotential and, ultimately, to unsuccessful performance. On the other hand, even though the cells charged to 4.1 V and 4.2 V did not evidence a significant difference regarding the resistance increase ratio, the cycling performance of those charged to 4.2 V was markedly better. Hence, the increase of the DC resistance was not the sole factor contributing to the cycling ageing of the cells. The present results indicate that, even if the resistance must be considered as a significant factor determining the best electrochemical conditions

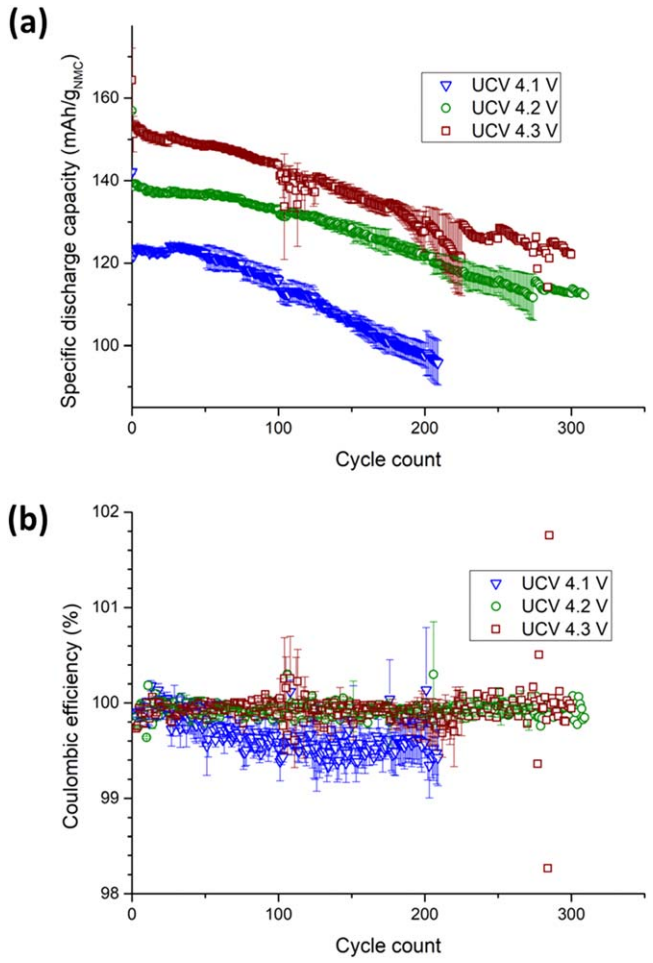

Figure 3. (a) Discharge capacity of the cells charged to 4.1 (blue triangles), 4.2 (green circles) and 4.3 V (red squares) with the number of cycles. (b) Average Coulombic efficiency of these cells.

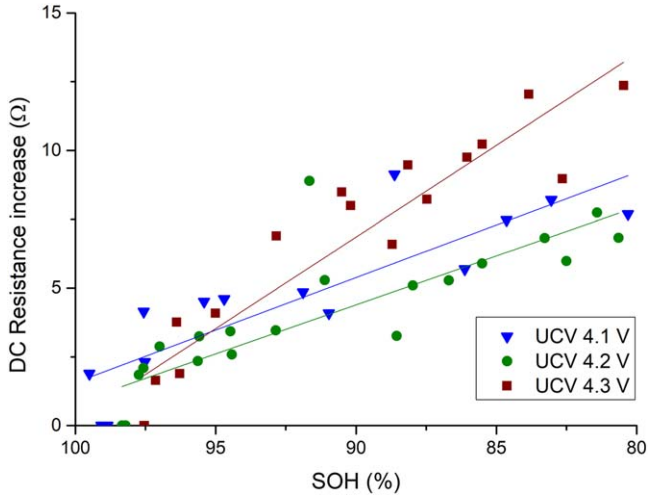

Figure 4. DC resistance evolution variation with respect to the SOH of the cells cycled with UCV 4.1 V (blue triangles), 4.2 V (green circles) and 4.3 V (red squares). Straight lines indicating linear trends are also included.

to maximize the performance of LIBs, a decreased DC resistance does not always guarantee an improved performance.

Electrochemical impedance spectroscopy (EIS) to monitor the origin of cell degradation.—EIS has been widely reported as a strategic diagnosis tool to determine the state of health of LIBs.[24,48–50] Impedance spectra between 10^6 and 10^{-3} Hz were recorded in the NMC622|graphite cells discharged down to 2.7 V every 25 cycles. The Bode plots obtained (an example is displayed in Fig. 5) show three main processes: one at high frequencies ($>10^3$ Hz, blue arrow in Fig. 5), another at mid-low frequencies (10^{-2} to 10 Hz, green arrow) and the last one at low frequencies ($<10^{-2}$ Hz, red arrow). The feature at high frequencies grows when the spectra before and after C/3 cycling are compared. Afterwards, it is maintained almost invariant during the subsequent scans and finally decreases by the end of life of the cell. Furthermore, the lack of symmetry of the curve at high frequency suggests an overlap of two contributions. On the other hand, the signal at mid-low frequencies is diminished with the number of cycles, also being shifted to higher frequencies. Finally, the feature at low frequencies is enhanced as cycling goes on. The identification, estimation and monitoring of the evolution of the different contributions in the impedance spectra can be done on the basis of an equivalent circuit. To do so, the corresponding Nyquist plots were also analyzed (Fig. S3).

As can be observed in Figs. S3b, S3c, the Nyquist diagrams were composed of two semicircles followed by a tail at low frequencies. The intersection of the curve with the *X*-axis is usually referred in the literature as the ohmic resistance of the cell. This contribution, identified as R0 in the equivalent circuit, is ascribed to the stability of the system, particularly the electrolyte, the separator, and the connections of the cell/wiring.[50–52] As the frequency decreases, the first semicircle is found between 10^6 and $10^{2.94}$ Hz, in good agreement with the feature at high frequencies in the Bode plot. Even though the previously discussed lack of symmetry of the feature in the Bode diagram is in good agreement with the use of two different resistances in order to fit this semicircle in the Nyquist plot, the use of multiple contributions to fit the data by a BMS in real LIBs could lead to complicate equivalent circuits which would difficult the fast evaluation of the state of the battery. Therefore, the semicircle was fitted with a resistance (R1) in parallel to a constant phase element (Q1).[53–56] The capacitance values associated to this element were between 10^{-5} and 10^{-7} F, suggesting a double-layer charging processes. Regarding the identification of this component, solid electrolyte interface (SEI) of the negative electrode has been recurrently assigned in literature to contributions appearing at this frequency range and capacitance values.[12,25,57] In this study, therefore, it is likely that R1 was generated because of this interface. Other processes such as the CEI[37,58] or the electrode-to-current collector interface[59] are also interfacial processes that could be associated to R1. Nevertheless, the magnitude of the SEI contribution is significantly higher than that of the CEI and contact resistances.[12,17,57,60] In this study, we have associated the evolution of R1 to the thickening of the SEI.

The feature observed at mid-low frequencies in the Bode plot is represented by the second semicircle in the Nyquist plot (frequencies between 10^1 and $10^{-1.56}$ Hz). This semicircle, can be fitted using a resistance in parallel to a CPE (R2Q2), and can be ascribed to a charge transfer resistance process. Finally, the tail at the lowest frequencies of the Nyquist plot ($10^{-1.56}$–10^{-3} Hz) corresponds with the signal discussed at such frequencies in the Bode diagram, and is widely ascribed in the literature to the diffusion in the solid particles. In the current equivalent circuit a Warburg element was used to simulate this process. All in all, the equivalent circuit built up to fit and analyze the evolution of the resistances of the different components, as well as an example of a fitted spectrum, are shown in Fig. 6. In addition, the evolution of the different resistances with the SOH is also displayed in this figure.

Overall, all the resistances showed a similar trend with the SOH, independently of the UCV. The ohmic resistance (R0) remained almost constant, between 0.5 and 2.5 Ω for all the cells in the analyzed SOH range (Fig. 6b). On the other hand, R1 (Fig. 6c), ascribed principally to the SEI and its growth, increased gradually with the SOH decrease, in good agreement with the continuous

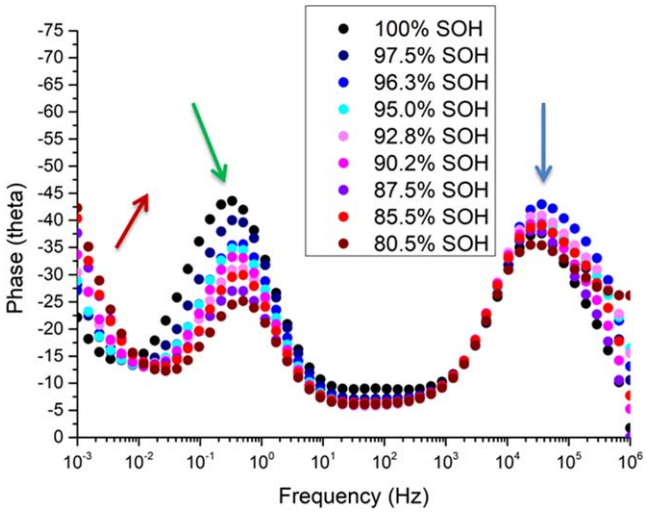

Figure 5. Example of the Bode plots recorded for a cell charged to 4.3 V at different percentage of SOH. The features at high (blue arrow), mid-low (green arrow) and low (red arrow) are highlighted in the Bode plot.

thickening of this layer reported in literature.[13,23,29] Regarding R2 (Fig. 6d), literature suggest that this contribution is associated with the charge transference in the bulk positive electrode;[61] the evolution of R2 follows an interesting trend: it is significantly decreased after the first scan, which can be associated with an activation process in the positive electrode[62] and/or the fracture of electronic insulating NMC particles[29] leading to a more efficient charge transfer. After that, it looks almost constant during the rest of the cycle life of the cell, in good agreement with Sun and Manthiram.[63] If R2 was the component leading to the capacity fade of the cell, an increase of the charge transfer in the bulk positive electrode could be expected with an increase of the cycles, as recently reported by Zhu et al.[29] In their work, the fracture of the NMC particles led to an increase in the surface area of the positive electrode materials, resulting in a heightened formation of NiO-like decomposition products. In our study, the SEM images of the NMC622 electrodes after cycling (Fig. S4) did not reveal an increased degradation of the positive electrode structure depending on the UCV, in good agreement with the similar charge transfer resistance values observed by the end of life of all the cells. Furthermore, the increase of R1, ascribed to the thickening of the SEI, implies the consumption of cyclable lithium. Thus, it would possibly involve a slightly lower degree of lithiation of the NMC622 electrode with the thickening of the SEI, leading to a lower charge transfer resistance at 0% SOC. On the other hand, in order to further evidence the correct identification of R2, the NMC622|Li HCC previously discussed in the Formation test to follow the reactions in the first cycle section was subjected to the same testing protocol of FCCs. The EIS spectra recorded every 25 cycles are displayed in Fig. S1. It can be appreciated the presence of a contribution similar to that at mid-low frequencies in full cell configuration.

It is worth to mention that the cells charged to 4.1 V presented the higher R1 overall value during all their cycle life, in spite of what could be expected: that charging the cell to a lower potential would lead to the formation of a thinner SEI and, hence, to a lower value of R1. However, it is well stablished that the building up of this interface is performed in different phases[23,32]: at the beginning of the formation charge, inorganic compounds such as Li_2O and LiF are generated in the electrode/electrolyte interface. Conversely, the SEI is enriched in organic compounds (polyolephines, organic (bi) carbonates) in the last stages of the charge. The later compounds provide mechanical stability to the SEI[23]; it is likely that the SEI layer formed at 4.1 V was not rich enough in these components, suffering cracking in the subsequent discharge (delithiation of the negative electrode). These cracks would promote the exposition of the graphite electrode to the electrolyte, which would lead to the formation of a more resistive SEI. In fact, the overall values of R1 of the cells with a UCV of 4.1 V were the highest during all the cycle life. This is also in good agreement with the lower coulombic efficiency of the LIBs charged to 4.1 V depicted in Fig. 3b, and outlines the importance of building up a robust SEI in order to achieve high cycling performance.[23,32,33] In order to provide further evidence of this hypothesis the post-mortem graphite electrodes of the studied cells were analyzed by means of XPS. The O1s and C1s regions of the scan for each of the electrodes are shown in Fig. 7. The assignation of features in the spectra was performed following the works published by Aurbach et al.,[64] Novák et al.[65] and Passerini et al.[32,66]

Deconvolution of the signal in the O 1s spectra revealed the presence of two main contributions, one with a maximum at 532.9 eV and the other at 534.8 eV. These two signals were ascribed to the formation of polyolephines/organic compounds and lithium carbonate (or alkyl carbonate). Thus, the former should be formed during the formation of the SEI, at higher potentials, while the latter is formed upon the thickening of the SEI, attributed to the ageing of the cell.[66] The area of the signal associated with carbonates (534.8 eV) with respect to that of polyolephines (532.9 eV) decreases with increasing the UCV (0.59, 0.55 and 0.47 CPS·eV for UCV = 4.1, 4.2 and 4.3 V, respectively), in good agreement with our previous assumption. Furthermore, the contribution at 284.4 eV in the C1s region is usually ascribed to C–C bonds of the graphite electrode[66]; hence, a thicker SEI would involve a decrease in the atomic contribution of this signal. In the electrodes analyzed, the atomic percentage of these peaks was 2.8%, 4.4% and 1.1% for UCV = 4.1, 4.2 and 4.3 V, respectively. The comparison of these values with those of R1 by the end of life of the cells shows a good correlation between the high resistance observed at 4.1 V in comparison to that at 4.2 V. Nevertheless, the low atomic percentage observed for the graphite electrode of the cell cycled with UCV = 4.3 V is not in good agreement with the resistance obtained in the fitting of the EIS spectra, which was similar to that of the cell charged to 4.2 V. This could be due to the low atomic percentage of this component compared to others close to it in the C1s spectra that could influence the quantification. On the other hand, signals associated with C–OR (285.9 eV), C=O (288 eV), COOR (290.5 eV) and C–F (291.9 eV) could also be deconvoluted. Moreover, the ratio between COOR (ascribed to the formation of carbonates) and C–O–C (related with polyolephines) followed the same trend previously described for the peaks in the O 1s spectra.

Coming back to the EIS data, this work pursues the in situ characterization of the LIBs during their cycle life. Therefore, the resistance variation ratio of the two main resistances (R1 and R2) was performed similarly to the DC resistance experiments. These two components are the main contributors to the resistance of the graphite (R1) and the NMC622 (R2) electrodes and can be used to analyze the evolution of each of them. In this case, the resistance values at different values of SOH were divided by the resistance obtained in the formation cycle. Figure 6e shows the evolution of R1 during the cycle life of the cells cycled setting the UCV at 4.1, 4.2 and 4.3 V. The slope of the regression line for each of the UCV reveals that R1 increases more severely as the cut-off potential is increased. As charge is prolonged the graphite electrode will intercalate more lithium, which will lead to a more pronounced expansion/contraction, enhanced cracking upon cycling, and ultimately to a thicker SEI. On the other hand, the evolution of R2 (Fig. 6f) does not show remarkable differences related to the UCV; all the samples undergo a marked decrease of this resistance by the beginning of the cycling life and are stabilized at approximately 80% of the initial value. Thus, it does not seem that the charge transference resistance in the bulk NMC622 material is significantly affected by the charge cut-off and this should not be the main factor affecting the cycle performance of the batteries. All in all, the cycle life seems to be more strongly related to the increase in the resistance of the SEI in the negative electrode, when UCV at 4.2 and 4.3 V are compared. In addition, the ineffective SEI formation in

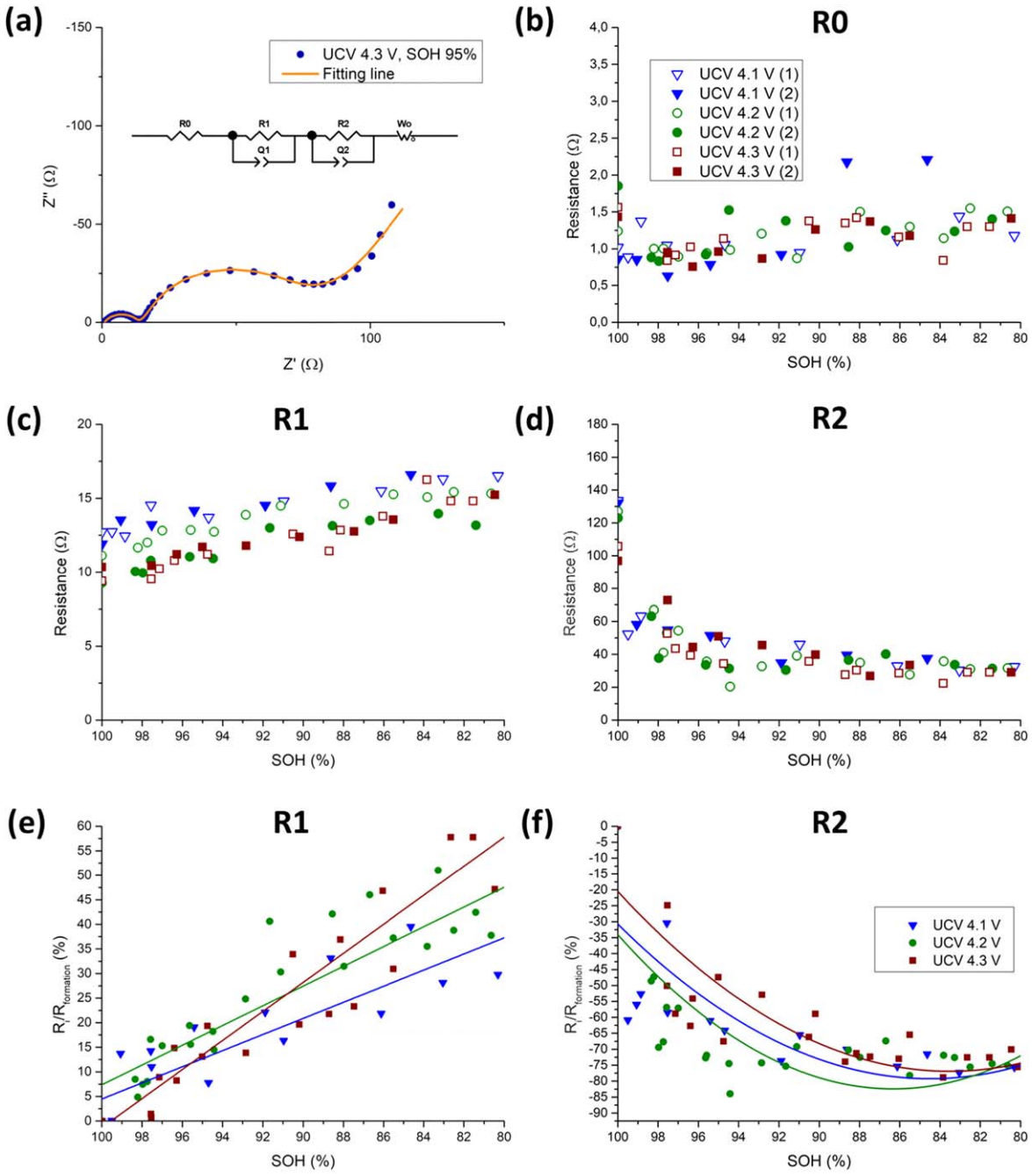

Figure 6. (a) An example of a Nyquist diagram and the corresponding fitting curve (inset: Equivalent circuit used to fit the impedance data of the LIBs). Evolution of the different resistances included in the equivalent circuit with the SOH. Resistances of the cells charged to 4.1 V (blue triangles), 4.2 V (green circles) and 4.3 V (red squares) are compared: (b) R0, (c) R1, and (d) R2. (e) R1 and (f) R2 variation evolution with the SOH.

the first cycle is reflected in the higher absolute value of R1 throughout the cycling life of the cell. Moreover, the DVA analysis in the upcoming section will provide further evidence on this hypothesis.

DVA to monitor the redox reactions upon cycling.—The dQ/dV vs voltage representation allows getting further detail of the distribution of the discharge or the charge reaction throughout the potential window. It is also useful to differentiate between reactions that are in some cases hardly detectable in the classical chronopotentiograms. In fact, as has been shown in Fig. 1 the reaction at 3.4 V during the discharge in the cell previously charged to 4.3 V could be determined by this method.

In the present work, a C/20 cycle was performed every 25 galvanostatic C/3 cycles in order to get further detail on the evolution of the reactions taking place in the LIB and analyze the influence of the UCV on these reactions. The DVA curves of the cells are presented in Fig. 8.

The dQ/dV vs voltage curves obtained in the formation cycle have been included in Fig. 8 (100% SOH) in order to compare them with the curves obtained throughout the cycling life of the LIBs. It can be observed that the three main features, c1, c2 and c3, occurred at lower overpotential, after the formation cycle, likely due to the activation occurred in the latter. In addition, the intensity of all the peaks decreased with the cycle life. It is worth mentioning that the c3 feature, ascribed to both the formation of the last part of the SEI and the M → H2 phase transition in the NMC, was significantly

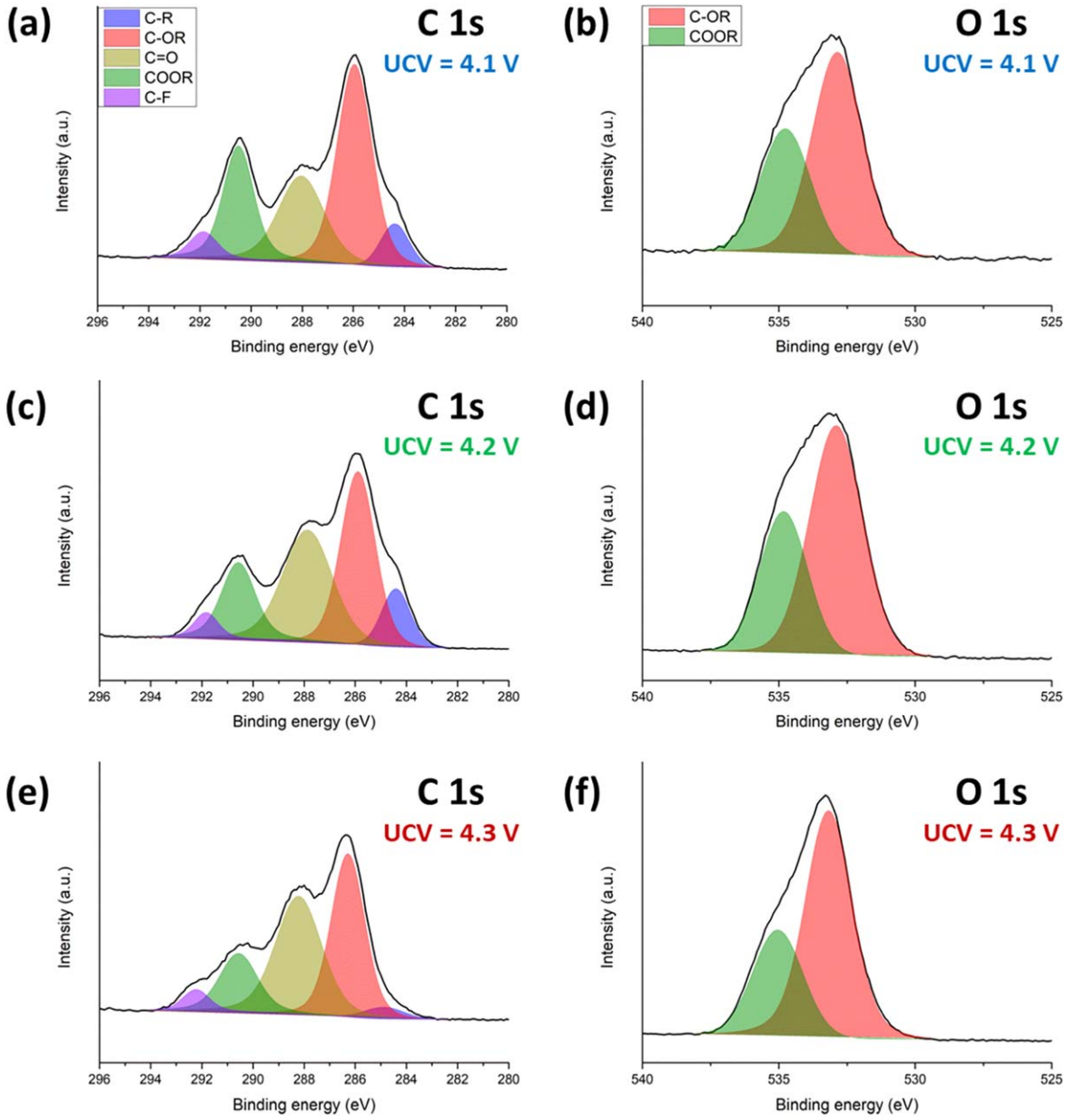

Figure 7. C 1s (left column) and O 1s (right column) XPS spectra for the graphite electrodes of the NMC622|graphite FCCs cycled until end of life setting as upper cut-off voltage (a), (b) 4.1, (c), (d) 4.2 and (e), (f) 4.3 V.

diminished after the formation cycle, evidencing the great contribution of the formation of the SEI on this peak in the first charge. Furthermore, this feature was gradually decreased with the number of cycles. Figure S5 shows the evolution of the intensity of this peak (normalized by its initial value) with the SOH.

As could be expected, the lower the UCV the more severely the evolution of the M → H2 transition was affected; the slope of the fitting line in Fig. S5 was lower with increasing the UCV, meaning that this transition was more successfully retained when the cell was charged to 4.3 V. On the other hand, this reaction occurred in a lower ratio after charging the cell to 4.1 V. In order to get further detail on this hypothesis, the NMC electrodes were analyzed by means of XRD after reaching the 80% SOH (XRD patterns and fittings are shown in Fig. S6). It has been reported that the M → H2 transition involves an extension of the c-parameter of the unit cell due to the repulsive forces of the negatively charged oxygen atoms.[19] The results of the XRD fitting are displayed in Fig. 9.

The NMC622 phase was fitted using the *R −3 m* hexagonal space group (JCPDS No. 00-85-1968, $Li_{0.89}Ni_{1.01}O_2$).[67] In addition, Al from the current collector (*F m −3 m*, cubic, JCPDS No. 03-65-2869) and graphite from the graphite fraction in the carbon black (*R −3 m*, hexagonal, JCPDS No. 01-73-5918) were included in the fitting.[68,69] As can be observed in Fig. 9, while *a* unit cell parameter did not undergo significant differences regardless the UCV selected, *c* was lower for the cell charged to 4.1 V (Fig. 9a). This evidences that, apart from the formation of a stable SEI, this phase transition was limited when the cell was cycled to 4.1 V. As could be expected, by increasing the charge cut-off voltage the cell volume was increased (Fig. 9b).

Regarding the discharge curves, it can be observed, as previously mentioned, the d1 peak corresponding to the delithiation of graphite appearing for all the cells, regardless the UCV, due to the off-set between the potential window of the electrodes. DVA of the discharges of the LIBs reveal that the feature observed at 3.4 V becomes more pronounced in the first cycles, with the maximum value for all samples after 50 cycles (97.53, 97.97 and 96.27% SOH for the cells charged to 4.1, 4.2 and 4.3 V, respectively), decreasing after that point. In parallel, the main feature, corresponding to the

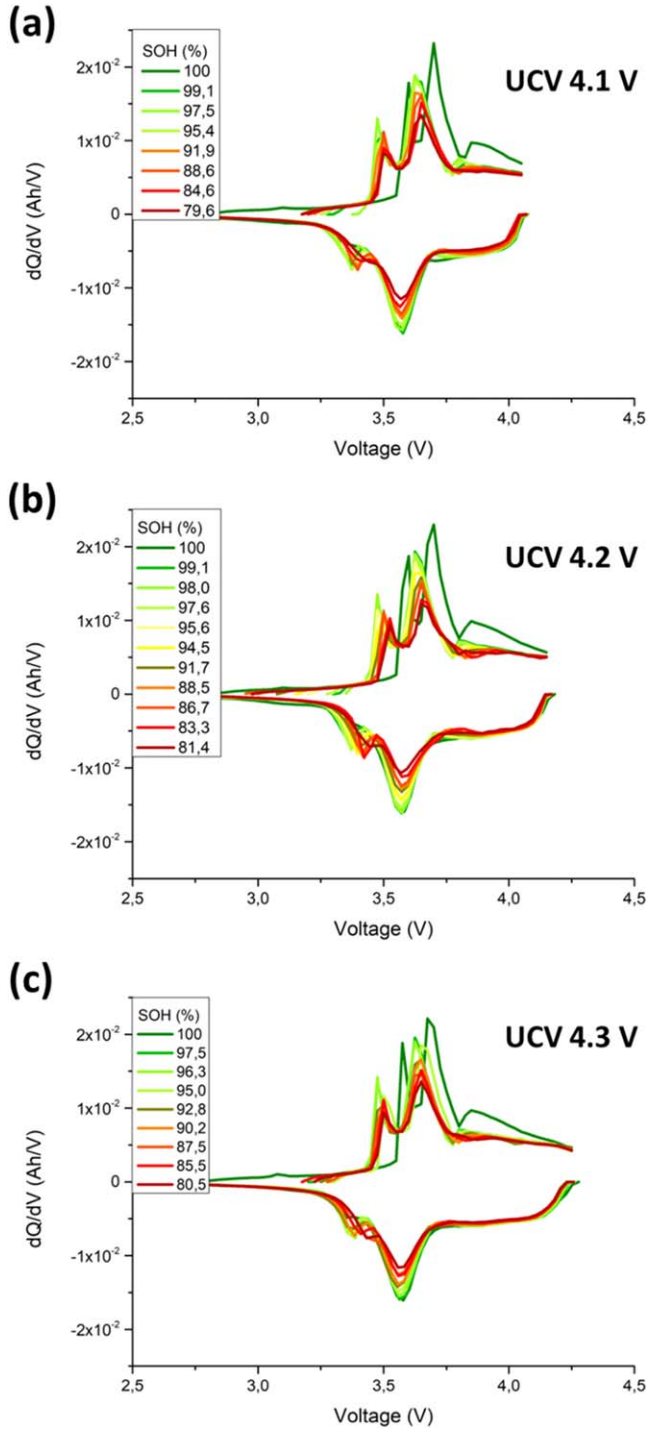

Figure 8. dQ/dV vs voltage curves recorded every 25 cycles for the cells charged to (a) 4.1, (b) 4.2 and (c) 4.3 V.

main plateau of the reaction at 3.6 V was diminished with decreasing SOH, in good agreement with the capacity loss experienced by the cell as their cycle life advanced. Interestingly, the minor peak (d1) was shifted towards higher potential and merged with the main signal at 3.6 V, which (opposite to what one could expect based on the resistance increase with the number of cycles previously discussed) did not show an increase of the overpotential during the cycling life of the cell, regardless the UCV selected. The decrease of the intensity of both cells is in good agreement with the loss of cyclable lithium ions; as the lithium ions available in the electrolyte are consumed (principally) in the continuous formation of the SEI

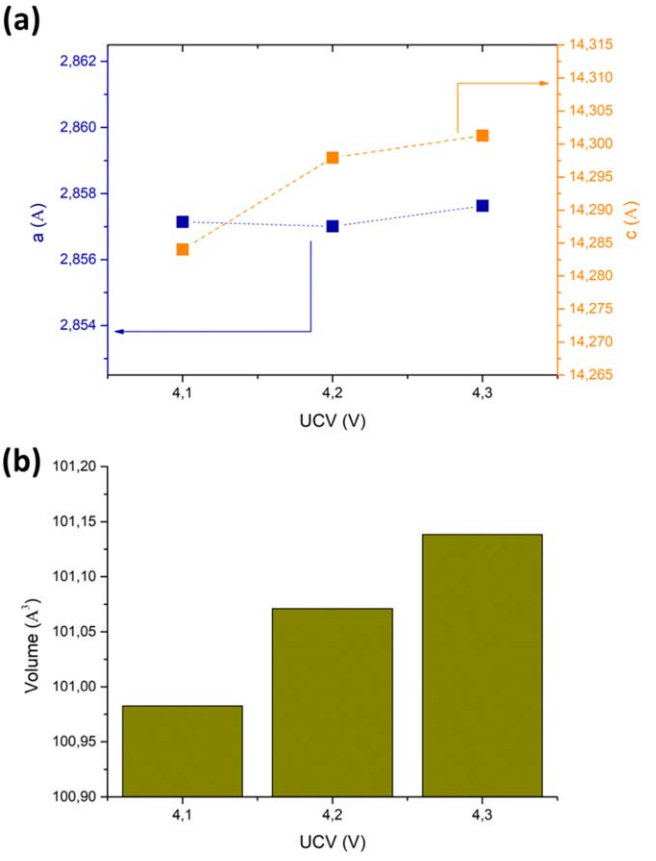

Figure 9. (a) Unit cell parameters and (b) volumes obtained by the XRD data fitting of the NMC622 positive electrodes charged to different cut-off voltages after reaching 80% of SOH.

(previously discussed in the EIS section), they cannot be used in the desired redox reactions in the electrodes anymore. Furthermore, by the end of the cycling life, the offset of the electrodes becomes negligible due to the lack of lithium to continue with the intercalation in the graphite electrode. Thus, the disappearance of the signal at 3.4 V can be designed as an indicative of the closeness to the end of life of the LIB.

Conclusions

In this work several in situ electrochemical characterization techniques have been applied to get information on the state of LIBs cycled at different upper cut-off voltages UCVs. Periodic measurements revealed that the increase of DC resistance during the cycle life of the cells was significantly enhanced with increasing the UCV. EIS analyses evidenced that this trend was in good agreement with the SEI resistance increase. On the other hand, it was observed that by limiting the charge of the cell to 4.1 V the SEI formed was not stable enough, resulting in an unsuccessful electrochemical performance. Furthermore, DVA experiments showed that the end of life of the cells occurred due to the loss of lithium inventory. The highest number of cycles was achieved for the cells charged to 4.2 V, while the highest amount of cumulative energy was obtained from the cells charged to 4.3 V.

Acknowledgments

The authors gratefully acknowledge Carmen Palacios from CIDETEC for the SEM measurements. In addition, the authors thank Dr. Oleksandr Bondarchuk from International Iberian Nanotechnology Laboratory (INL) for the XPS measurements.

ORCID

Imanol Landa-Medrano https://orcid.org/0000-0003-4180-5262
Iratxe de Meatza https://orcid.org/0000-0001-8245-5815

References

1. M. Li, J. Lu, Z. Chen, and K. Amine, *Adv. Mater.*, **30**, 1800561 (2018).
2. Y. Li, J. Yang, and J. Song, *Renew. Sustain. Energy Rev.*, **74**, 19 (2017).
3. J. B. Goodenough and Y. Kim, *Chem. Mater.*, **22**, 587 (2010).
4. M. Winter, B. Barnett, and K. Xu, *Chem. Rev.*, **118**, 11433 (2018).
5. Y. Jin, B. Zhu, Z. Lu, N. Liu, and J. Zhu, *Adv. Energy Mater.*, **7**, 1700715 (2017).
6. J. Liu et al., *Nat. Energy*, **4**, 180 (2019).
7. P. K. Nayak, E. M. Erickson, F. Schipper, T. R. Penki, N. Munichandraiah, P. Adelhelm, H. Sclar, F. Amalraj, B. Markovsky, and D. Aurbach, *Adv. Energy Mater.*, **8**, 1702397 (2018).
8. R. T. Jow, K. Xu, O. Borodin, and M. Ue, *Electrolytes for Lithium and Lithium-Ion Batteries* (Springer-Verlag, New York) (2014).
9. A. Tornheim, S. Sharifi-Asl, J. C. Garcia, J. Bareño, H. Iddir, R. Shahbazian-Yassar, and Z. Zhang, *Nano Energy*, **55**, 216 (2019).
10. X.-G. Yang, T. Liu, Y. Gao, S. Ge, Y. Leng, D. Wang, and C.-Y. Wang, *Joule*, **3**, 3002 (2019).
11. A. S. Mussa, A. Liivat, F. Marzano, M. Klett, B. Philippe, C. Tengstedt, G. Lindbergh, K. Edström, R. W. Lindström, and P. Svens, *J. Power Sources*, **422**, 175 (2019).
12. R. Raccichini, M. Amores, and G. Hinds, *Batteries*, **5**, 12 (2019).
13. X. Ma, J. E. Harlow, J. Li, L. Ma, D. S. Hall, S. Buteau, M. Genovese, M. Cormier, and J. R. Dahn, *J. Electrochem. Soc.*, **166**, A711 (2019).
14. N. Laszczynski, S. Solchenbach, H. A. Gasteiger, and B. L. Lucht, *J. Electrochem. Soc.*, **166**, A1853 (2019).
15. A. Rezqita, A.-R. Kathribail, J. Kahr, and M. Jahn, *J. Electrochem. Soc.*, **166**, A5483 (2019).
16. W. Li, E. M. Erickson, and A. Manthiram, *Nat. Energy*, **5**, 26 (2020).
17. K. Redel, A. Kulka, A. Plewa, and J. Molenda, *J. Electrochem. Soc.*, **166**, A5333 (2019).
18. Y. Mao et al., *Adv. Funct. Mater.*, **29**, 1900247 (2019).
19. R. Jung, M. Metzger, F. Maglia, C. Stinner, and H. A. Gasteiger, *J. Electrochem. Soc.*, **164**, A1361 (2017).
20. D. Leanza, M. Mirolo, C. A. F. Vaz, P. Novak, and M. El Kazzi, *Batter. Supercaps*, **2**, 482 (2019).
21. T. Plattard, N. Barnel, L. Assaud, S. Franger, and J.-M. Duffault, *Batteries*, **5**, 36 (2019).
22. A. Mauger, C. M. Julien, J. B. Goodenough, and K. Zaghib, *J. of the Electrochem. Soc.*, **167**, 070507 (2020).
23. E. Peled and S. Menkin, *J. Electrochem. Soc.*, **164**, A1703 (2017).
24. A. Schmidt, A. Smith, and H. Ehrenberg, *J. Power Sources*, **425**, 27 (2019).
25. G. Bieker, M. Winter, and P. Bieker, *Phys. Chem. Chem. Phys.*, **17**, 8670 (2015).
26. C. Mao, S. J. An, H. M. Meyer III, J. Li, M. Wood, R. E. Ruther, and D. L. Wood III, *J. Power Sources*, **402**, 107 (2018).
27. F. Farmakis, C. Elmasides, P. Selinis, and N. Georgoulas, *Electrochim. Acta*, **245**, 99 (2017).
28. I. D. Campbell, M. Marzook, M. Marinescu, and G. J. Offer, *J. Electrochem. Soc.*, **166**, A725 (2019).
29. J. Zhu et al., *J. Power Sources*, **448**, 227575 (2020).
30. I. Zilberman, J. Sturm, and A. Jossen, *J. Power Sources*, **425**, 217 (2019).
31. S. J. An, J. Li, Z. Du, C. Daniel, and D. L. Wood, *J. Power Sources*, **342**, 846 (2017).
32. A. Moretti, V. Sharova, D. V. Carvalho, A. Boulineau, W. Porcher, I. de Meatza, and S. Passerini, *Batter. Supercaps*, **2**, 240 (2019).
33. D. L. Wood, J. Li, and S. J. An, *Joule*, **3**, 2884 (2019).
34. M. Wetjen, M. Trunk, L. Werner, R. Gernhäuser, B. Märkisch, Z. Révay, R. Gilles, and H. A. Gasteiger, *J. Electrochem. Soc.*, **165**, A2340 (2018).
35. S. Madani, E. Schaltz, and S. Knudsen Kær, *Batteries*, **5**, 31 (2019).
36. P. Shafiei Sabet and D. U. Sauer, *J. Power Sources*, **425**, 121 (2019).
37. R. Tatara, P. Karayaylali, Y. Yu, Y. Zhang, L. Giordano, F. Maglia, R. Jung, J. Philipp Schmidt, I. Lund, and Y. Shao-Horn, *J. Electrochem. Soc.*, **166**, A5090 (2018).
38. T. Q. Nguyen and C. Breitkopf, *J. Electrochem. Soc.*, **165**, E826 (2018).
39. F. Paloukis, C. Elmasides, F. Farmakis, P. Selinis, S. G. Neophytides, and N. Georgoulas, *J. Power Sources*, **331**, 285 (2016).
40. J. Rodríguez-Carvajal, *Phys. B Phys. Condens. Matter*, **192**, 55 (1993).
41. H. Zhang et al., *Angew. Chemie Int. Ed.*, **59**, 534 (2020).
42. L. de Biasi, B. Schwarz, T. Brezesinski, P. Hartmann, J. Janek, and H. Ehrenberg, *Adv. Mater.*, **31**, 1900985 (2019).
43. S. Gantenbein, M. Schönleber, M. Weiss, and E. Ivers-Tiffée, *Sustainability*, **11**, 6697 (2019).
44. C. M. Julien and A. Mauger, *AIMS Mater. Sci.*, **5**, 650 (2018).
45. K. G. Gallagher, D. W. Dees, A. N. Jansen, D. P. Abraham, and S. H. Kanga, *J. Electrochem. Soc.*, **159**, A2029 (2012).
46. M. D. Levi and D. Aurbach, *J. Electroanal. Chem.*, **421**, 79 (1997).
47. V. Murray, D. S. Hall, and J. R. Dahn, *J. Electrochem. Soc.*, **166**, A329 (2019).
48. T. Momma, M. Matsunaga, D. Mukoyama, and T. Osaka, *J. Power Sources*, **216**, 304 (2012).
49. S. D. Talian, J. Bobnar, A. R. Sinigoj, I. Humar, and M. Gaberscek, *J. Phys. Chem. C*, **123**, 27997 (2019).
50. H. Dai, B. Jiang, and X. Wei, *Energies*, **11**, 220 (2018).
51. M. Tokur, A. Aydin, T. Cetinkaya, and H. Akbulut, *J. Electrochem. Soc.*, **164**, A2238 (2017).
52. S.-B. Son, L. Cao, T. Yoon, A. Cresce, S. E. Hafner, J. Liu, M. Groner, K. Xu, and C. Ban, *Adv. Sci.*, **6**, 1801007 (2018).
53. I. Landa-Medrano, J. T. Frith, I. Ruiz de Larramendi, I. Lozano, N. Ortiz-Vitoriano, N. Garcia-Araez, and T. Rojo, *J. Power Sources*, **345**, 237 (2017).
54. I. Landa-Medrano, I. Ruiz de Larramendi, N. Ortiz-Vitoriano, R. Pinedo, J. I. Ruiz de Larramendi, and T. Rojo, *J. Power Sources*, **249**, 110 (2014).
55. J. R. Macdonald, *Solid State Ionics*, **13**, 147 (1984).
56. V. Ovejas and A. Cuadras, *Batteries*, **4**, 43 (2018).
57. D. W. Abarbanel, K. J. Nelson, and J. R. Dahn, *J. Electrochem. Soc.*, **163**, A522 (2016).
58. X. Li, A. M. Colclasure, D. P. Finegan, D. Ren, Y. Shi, X. Feng, L. Cao, Y. Yang, and K. Smith, *Electrochim. Acta*, **297**, 1109 (2019).
59. D. Pritzl, A. E. Bumberger, M. Wetjen, J. Landesfeind, S. Solchenbach, and H. A. Gasteiger, *J. Electrochem. Soc.*, **166**, 582 (2018).
60. M. D. Murbach and D. T. Schwartz, *J. Electrochem. Soc.*, **165**, A297 (2018).
61. T. Momma, T. Yokoshima, H. Nara, Y. Gima, and T. Osaka, *Electrochim. Acta*, **131**, 195 (2014).
62. R. Fu, X. Zhou, H. Fan, D. Blaisdell, A. Jagadale, X. Zhang, and R. Xiong, *Energies*, **10**, 2174 (2017).
63. H. H. Sun and A. Manthiram, *Chem. Mater.*, **29**, 8486 (2017).
64. D. Aurbach, E. Pollak, R. Elazari, G. Salitra, C. S. Kelley, and J. Affinito, *J. Electrochem. Soc.*, **156**, 694 (2009).
65. A. Guéguen, P. Novák, and E. J. Berg, *J. Electrochem. Soc.*, **163**, A2545 (2016).
66. A. Moretti, D. V. Carvalho, N. Ehteshami, E. Paillard, W. Porcher, D. Brun-Buisson, J. B. Ducros, I. de Meatza, A. Eguia-Barrio, K. Trad, and S. Passerini, *Batteries*, **5**45 (2019).
67. Q. Wang, C.-H. Shen, S.-Y. Shen, Y.-F. Xu, C.-G. Shi, L. Huang, J.-T. Li, and S.-G. Sun, *ACS Appl. Mater. Interfaces*, **9**, 24731 (2017).
68. P. M. Attia, S. Das, S. J. Harris, M. Z. Bazant, and W. C. Chueh, *J. Electrochem. Soc.*, **166**, E97 (2019).
69. A. Rezqita, R. Hamid, S. Schwarz, H. Kronberger, and A. Trifonova, *ECS Trans.*, **66**, 17 (2015).